nature physics

ARTICLES

https://doi.org/10.1038/s41567-022-01688-8

Check for updates

Flagella-like beating of actin bundles driven by self-organized myosin waves

Marie Pochitaloff[1,9], Martin Miranda[2], Mathieu Richard[1], Atitheb Chaiyasitdhi[1], Yasuharu Takagi[3], Wenxiang Cao[4], Enrique M. De La Cruz[4], James R. Sellers[3], Jean-François Joanny[1,5], Frank Jülicher[2,6], Laurent Blanchoin[7,8] and Pascal Martin[1]✉

Wave-like beating of eukaryotic cilia and flagella—threadlike protrusions found in many cells and microorganisms—is a classic example of spontaneous mechanical oscillations in biology. This type of self-organized active matter raises the question of the coordination mechanism between molecular motor activity and cytoskeletal filament bending. Here we show that in the presence of myosin motors, polymerizing actin filaments self-assemble into polar bundles that exhibit wave-like beating. Importantly, filament beating is associated with myosin density waves initiated at twice the frequency of the actin-bending waves. A theoretical description based on curvature control of motor binding to the filaments and of motor activity explains our observations in a regime of high internal friction. Overall, our results indicate that the binding of myosin to actin depends on the actin bundle shape, providing a feedback mechanism between the myosin activity and filament deformations for the self-organization of large motor filament assemblies.

Biological systems can self-organize at large scales by orchestrating the local activity of many small constituents that each consume energy from the environment. The regular beating patterns exhibited by cilia and flagella provide a prototypical example of such self-organization. Using an in vitro biomimetic approach, we study here the minimum requirements needed for the emergence of the spontaneous beating of polar bundles of biofilaments driven by molecular motors.

The cilia and flagella of eukaryotes ranging from single cells to complex organisms share a complex common structure—the axoneme. The axoneme comprises a cylindrical arrangement of parallel filaments called microtubules, about 10,000 dynein motors uniformly distributed along the microtubules[1,2], as well as hundreds of other proteins[3]. Importantly, the flagellar beat—a regular oscillatory pattern of propagating bending waves—requires the coordination of motors both in time and along the length of the axoneme[2,4,5]. The dynamics of flagellar beating is a classical problem of theoretical biophysics. Many models have been developed to describe the feedback mechanisms specifying how the activity of the molecular motors depends on the filament bundle shape[4–13]. However, the coupling between motor activity and flagellar beating is still a matter of debate[2]. In addition, although dissipation from external hydrodynamic drag on the flagellar outer surface is usually thought to balance the power input from the motors, the contribution of internal sources of friction has recently been discussed[14–16].

Biomimetic in vitro experiments with purified proteins[17–19] have demonstrated that spontaneous oscillations can emerge in motor ensembles under elastic loading, without the intervention of regulatory proteins or the external drive of an oscillatory biochemical signal. These experiments confirmed the predicted existence of generic oscillatory instabilities in motor systems[11,20,21]. In contrast to top-down approaches on functional cilia or flagella, in vitro experiments afford an attractive means to control physical parameters such as the size of the system, geometrical constraints or the properties of the motors at work and thus to probe the physical underpinning of motor coordination in oscillatory systems.

In this work, we present a bottom-up approach based on a minimal active molecular system. We show that in the presence of myosin motors, polymerizing actin filaments can self-assemble in vitro into polar bundles of filaments that spontaneously exhibit wave-like beating. The beating properties in this artificial system resemble those of eukaryotic flagella, despite the different molecular identities of the filaments and motors at work and despite the lack of regulatory proteins. We used surface micropatterns of actin nucleators to control the geometry of actin bundle formation in the presence of myosin motors. We analysed the properties of the emerging actin-bending waves as a function of the size of the actin bundle and of the identity of the myosin motors that drive the oscillations. Importantly, we demonstrate that actin-bending waves are associated with myosin density waves: myosin recruitment and localization on the actin bundle are dynamically coupled to the actin bundle shape. A theoretical description based on curvature control of motor binding to the filaments and of motor activity explains our observations in a regime of high internal friction.

Results

We used surface micropatterns—disks—of a nucleation-promoting factor to control the geometry and collective organization of actin

[1]Laboratoire Physico-Chimie Curie, Institut Curie, Université PSL, Sorbonne Université, CNRS UMR168, Paris, France. [2]Max Planck Institute for the Physics of Complex Systems, Dresden, Germany. [3]Laboratory of Molecular Physiology, National Heart, Lung and Blood Institute, NIH, Bethesda, MD, USA. [4]Department of Molecular Biophysics and Biochemistry, Yale University, New Haven, CT, USA. [5]Collège de France, Paris, France. [6]Cluster of Excellence Physics of Life, Technische Universität Dresden, Dresden, Germany. [7]CytomorphoLab, Biosciences and Biotechnology Institute of Grenoble, Laboratoire de Physiologie Cellulaire & Végétale, Université Grenoble-Alpes/CEA/CNRS/INRA, Grenoble, France. [8]CytomorphoLab, Hôpital Saint Louis, Institut Universitaire d'Hématologie, UMRS1160, INSERM/AP-HP/Université Paris Diderot, Paris, France. [9]Present address: Department of Mechanical Engineering, UC Santa Barbara, Santa Barbara, CA, USA. ✉e-mail: pascal.martin@curie.fr

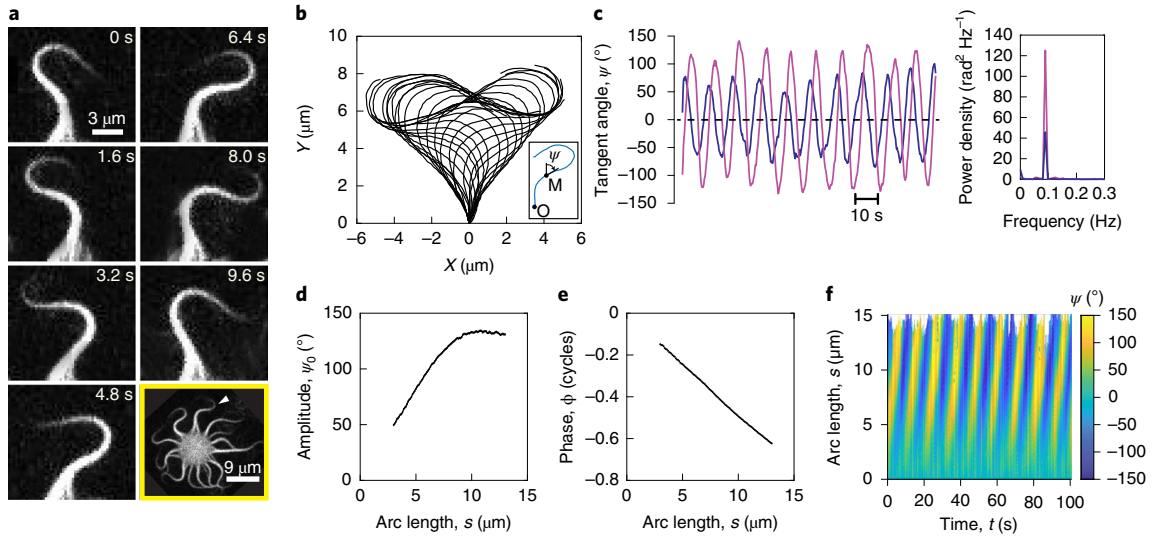

Fig. 1 | Beating of an actin filament bundle with myosin II. a, Snapshots of the actin filament bundle. The yellow box shows that the bundle (arrowhead) has grown to length $L = 14.8\,\mu m$ from a micropatterned, actin nucleation disk. **b**, Beating pattern resulting from the automatic tracking of the bundle's centre line (same bundle as in **a**). The inset defines the tangent angle ψ at any point M of a bundle's centre line; the arc-length origin $s = 0$ is at the bundle's base (point O). **c**, Tangent angle $\psi(t, s)$ as a function of time t at the arc lengths $s = 5\,\mu m$ (purple) and $s = 10\,\mu m$ (magenta); the corresponding power-spectral densities are shown on the right and their peaks indicate an oscillation period $T = 11.2\,s$. **d**, Amplitude $\psi_0(s) = \sqrt{2\langle(\psi(t,s) - \langle\psi(t,s)\rangle)^2\rangle}$ of the tangent angle oscillation as a function of arc length s. The growth rate in the linear portion of the curve is $\psi_0' = 16.2\,°\,\mu m^{-1}$. **e**, Phase ϕ of the Fourier amplitude at the beating frequency as a function of arc length s. The slope to a linear fit to the relationship $\phi(s)$ provides the wavevector $q = 0.30\,rad\,\mu m^{-1}$, corresponding to the wavelength $\lambda = 20.9\,\mu m$ and propagation velocity $v = \lambda/T = 1.9\,\mu m\,s^{-1}$ of the actin-bending waves. **f**, Colour plot of the tangent angle $\psi(t, s)$ as a function of time t and arc length s.

polymerization[22–24]. Because of steric interactions, actin filaments grow perpendicular to the circular borders of the actin nucleation zone by monomer addition to their barbed ends, resulting in radial polar networks of filaments (Extended Data Fig. 1). Previous work has demonstrated that the length of the actin filaments is exponentially distributed, with a mean length of about 8 μm (ref. [24]). The inclusion of a depleting agent ensured that most of the filaments grew parallel to the substrate and that the network remained within a few hundred nanometres of the passivated glass surface[25]; the depleting agent also facilitated bundle formation[26]. We performed the in vitro polymerization assay in the presence of either heavy meromyosin II, which is a soluble two-headed fragment of skeletal muscle myosin II (hereafter called myosin II for simplicity), or of a two-headed fragment of myosin Va fused to the green fluorescent protein (GFP; hereafter called myosin V). We found that growing actin filaments in the presence of myosin motors self-organized into bundles with a diameter that decreased from their proximal to their distal ends (Extended Data Fig. 1). Remarkably, the actin filament bundles displayed periodic bending waves travelling from the base towards the tip of the bundle (Extended Data Fig. 1 and Supplementary Videos 1–3). In the following, index 'II' and 'V' refer to data obtained with myosin II and myosin V motors, respectively. Unless otherwise indicated, we provide the average and standard deviation (s.d.) values of beating bundle properties over ensembles of n bundles.

Actin-bending waves driven by myosin II. We analysed the beating properties of fluorescently labelled actin bundles after 23 ± 8 min (mean ± s.d.; $n = 59$) of polymerization. At this time, the bundles had grown to a length $L_{II} = 15.9 \pm 6.1\,\mu m$ ($n = 59$). Automatic tracking of the centre line of an actin filament bundle (Fig. 1a and Supplementary Video 4) revealed beating patterns with a heart-shaped envelope in which the bundle's tip follows a characteristic figure-of-eight pattern (Fig. 1b). These patterns resemble those reported for flagella of the bull sperm[27,28] but with slower beating kinetics. At any given arc length s, the angle $\psi(t, s)$ between the tangent to the bundle's centre line and the vertical axis (Fig. 1c, Y axis) displayed sinusoidal oscillations as a function of time t (Fig. 1c,d) with a period $T_{II} = 15 \pm 9\,s$ ($n = 59$). The oscillation amplitude ψ_0 increased linearly from the base of the bundle to typically two-thirds the total length at the rate $\psi_0' = 12.5 \pm 3.4\,°\,\mu m^{-1}$ ($n = 59$), before saturating (Fig. 1d) and reaching a maximum value $\psi_{MAX} = 127 \pm 11°$ ($n = 46$). Saturation was observed only when the bundle was long enough, typically $L_{II} > 11\,\mu m$ (Extended Data Fig. 2). The phase $\phi(s)$ of tangent angle oscillation decreased from the base ($s = 0$) to the tip ($s = L$) of the bundle, with a nearly linear relationship of slope ϕ' over most of the bundle's length (Fig. 1e). As a result, the wavelength $\lambda_{II} = -2\pi/\phi' = 17.1 \pm 5.8\,\mu m$ ($n = 59$) and velocity $v_{II} = \lambda_{II}/T_{II} = 1.4 \pm 0.8\,\mu m\,s^{-1}$ ($n = 59$) of the corresponding travelling wave were nearly uniform along the bundle. A colour plot of $\psi(t, s)$ recapitulates these observations; propagation of actin-bending waves at uniform velocities is visualized by linear isocolour lines (Fig. 1f). Wave propagation at uniform velocities is remarkable considering that the actin bundles are about 1 μm thick near their base, where they comprise hundreds of filaments, and get progressively thinner towards their tip, where they end with a single or only a few filaments. As discussed in the Supplementary Information, bending-wave propagation at uniform velocity despite the structural heterogeneity of the filament bundle is most easily explained if an internal source of friction dominates external viscous drag on the bundle. Uniform wave velocities are also often observed in eukaryotic flagellar systems[5], but these flagella are based on a homogeneous axonemal structure comprising nine doublets of microtubules along most of the flagellar length.

The actin filament bundles generally remained in focus within the observation plane of the spinning-disk microscope, indicating that the beating motion was almost planar. However, weak blinking of the actin fluorescence intensity at a given arc length betrayed a

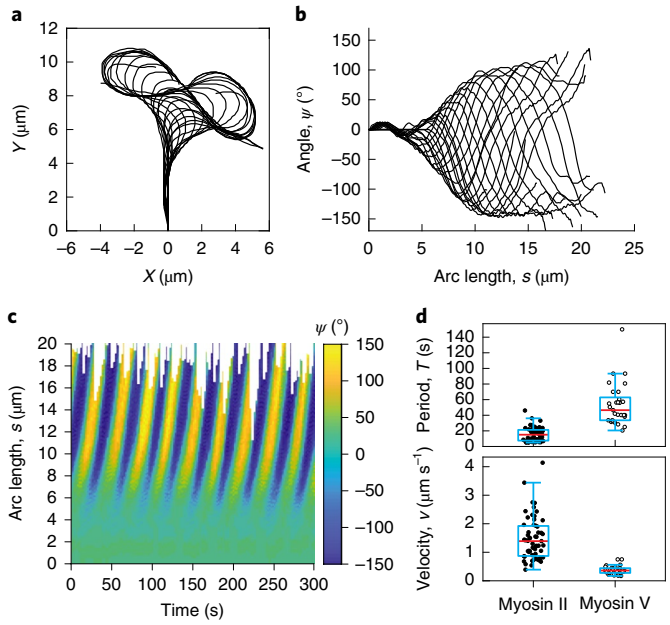

Fig. 2 | Beating of an actin filament bundle with myosin V. a, Beating pattern. **b**, Tangent angle profile $\psi(s)$ (defined in Fig. 1b) at various times over one period of oscillation, with a 2-s time interval between successive profiles. **c**, Colour plot of tangent angle $\psi(t,s)$ as a function of time t and arc length s. Here the period of tangent angle oscillation is $T=30.6$ s and the actin filament bundle has an average visible length $L=18$ μm. **d**, Box plots (25th and 75th percentiles in cyan; median values in red; whiskers indicate the maximum and minimum values that are not considered as outliers, corresponding to deviations below the lower quartile and above the upper quartile by less than 1.5 times the interquartile range, respectively) and data points for the period T of tangent angle oscillations (top) and velocity v of bending waves (bottom) driven by myosin II (black disks) and myosin V (white disks).

small out-of-plane component to the beat that could result in oscillations of the projected bundle length (Extended Data Fig. 3 and Supplementary Video 5). We analysed here the shape of the beat pattern within the plane of the beat.

Actin-bending waves driven by myosin V. To evaluate the generality of self-organized beating in polar bundles of actin filaments driven by myosin motors, we also performed experiments with myosin V motors. Both myosin II and myosin V are double-headed molecular motors with movements directed towards the barbed ends of the actin filaments and thus away from the nucleation disks of actin polymerization. However, their biophysical properties and in vivo functions differ strongly[29]: myosin II is a non-processive motor that normally works in large groups to mediate muscle contraction, whereas myosin V is a processive motor that usually operates at the level of a single dimer or a few dimers.

Despite these differences, we found that polar actin networks could also self-assemble into wave-like beating bundles under the action of myosin V (Fig. 2 and Supplementary Videos 2 and 3). The heart-shaped beating patterns and figure-of-eight patterns with myosin V were similar to those obtained with myosin II. Over an ensemble of $n=29$ beating bundles of length $L_V=18.3\pm5.4$ μm, actin-bending waves of wavelength $\lambda_V=15.9\pm3.5$ μm travelled at nearly uniform velocities from the bundle's base towards its tip, whereas the amplitude ψ_0 of tangent angle oscillations grew along the length of the bundle at a rate $\psi_0'=18.9\pm3.6\,°\,\mu m^{-1}$ before reaching a maximum value $\psi_{MAX}=133\pm11°$. There was no statistical difference between the mean values of the bundle length and wavelength for myosin II and myosin V motors, but the amplitude of tangent angle oscillation increased more steeply with the arc length and the maximum tangent angle was slightly larger for myosin V (Table 1). The most striking difference between the two motor types was in the kinetics of the beating movements. Myosin V is known to be a slower motor than myosin II (ref. [30]). Accordingly, tangent angle oscillations and the propagation of actin-bending waves were about fourfold slower with myosin V (Fig. 2d and Table 1), corresponding to the period $T_V=54\pm27$ s ($n=29$) and travelling-wave velocity $v_V=0.37\pm0.15\,\mu m\,s^{-1}$ ($n=29$).

Effects of bundle length on beating properties. We observed the self-organized beating of actin filament bundles with a length L that ranged between 6 and 40 μm. Over this range, the wavelength λ of the bending waves displayed a positive correlation with the bundle length (Fig. 3a), both with myosin II (Pearson's test; $r=0.72$; p value, 1.7×10^{-10}) and with myosin V (Pearson's test; $r=0.36$; p value, 1.1×10^{-3}). Longer bundles showed longer wavelengths and the wavelength was, on average, nearly equal to the bundle length (Table 1). In ensemble averages, the oscillation period of the tangent angle displayed a weak positive correlation with the bundle length with myosin V (Pearson's test; $r=0.36$; p value$=0.05$) but no significant correlation with myosin II (Pearson's test; $r=0.20$; p value$=0.13$). However, because the beating actin bundles elongated at a velocity of $0.8\pm0.5\,\mu m\,min^{-1}$ ($n=14$) as polymerization proceeded, our in vitro assay provides an attractive means to probe, in a single experiment, how the beating properties change with the bundle length as all other parameters remained fixed (Fig. 3b,c and Supplementary Video 6). With myosin II, beating was fast enough that the actin bundle length remained nearly constant over a few tens of oscillation cycles (Fig. 3b). In this case, we observed that the period of tangent angle oscillation increased with the bundle's length at a mean rate of $0.9\pm0.7\,s\,\mu m^{-1}$ ($n=5$). In agreement with the observed increase in wavelength with bundle length (Fig. 3a), the travelling velocity of the actin-bending waves stayed nearly the same over the range of bundle length that we could explore (Fig. 3c, inset).

Interplay between actin-bending and myosin density waves. Because myosin V was fused to the GFP, we could visualize the motors during the wave-like beating of actin bundles (Supplementary Videos 7–9). In contrast to the monotonically decreasing and stationary actin density profiles (Extended Data Fig. 4a), the myosin density profiles exhibited a peak that appeared abruptly near the bundle's base and then travelled towards the bundle's tip, corresponding to a myosin density wave (Fig. 4a). Thus, although they were added in bulk at a homogeneous concentration, the motors did not decorate the actin bundle according to the local actin density but were instead enriched within an apical region of the bundle. The myosin fluorescence signal was elongated, conformed to the local shape of the bundle, and thus followed the bundle movement (Extended Data Fig. 5a). The myosin density peak remained within a restricted region of the observation plane near the centre of the figure-of-eight pattern drawn by the bundle's tip (Extended Data Fig. 5b). As a result, when the beating bundle grew in length, the myosin density peak moved together with the figure-of-eight pattern (Supplementary Video 9 and Extended Data Fig. 5c,d). Interestingly, plotting the ratio of myosin and actin density profiles revealed an increase in the motor density per actin filament during wave propagation (Extended Data Fig. 4b). The arc length at which the myosin density was maximum (Fig. 4d,e) displayed a sawtooth-shaped oscillation as a function of time. These observations suggest that myosin motors were periodically recruited in a proximal region of the filament bundle and released at the bundle's tip.

To describe how the myosin density waves were coupled to the underlying actin-bending waves, we compared the myosin density profiles (Fig. 4a,d) with the bundle curvature profiles (Fig. 4b,c and

Table 1 | Beating characteristics and statistical testing

Parameter	Definition	Myosin II ($n=59$)	Myosin V ($n=29$)	Statistical t-test
L (μm)	Bundle length	15.9 ± 6.1	18.3 ± 5.4	n.s.
λ (μm)	Wavelength of bending waves	17.1 ± 5.8	15.9 ± 3.5	n.s.
λ/L	Wavelength–length ratio	1.1 ± 0.3	0.9 ± 0.3	**
ψ_0' (° μm^{-1})	Growth rate of tangent angle oscillation	12.5 ± 3.4	18.9 ± 3.6	****
ψ_{MAX} (°)	Maximum tangent angle	127 ± 11	133 ± 11	*
T (s)	Tangent angle period	15 ± 9	54 ± 27	****
v (μm s^{-1})	Bending-wave velocity	1.4 ± 0.8	0.37 ± 0.15	****

The numerical values are given as mean ± s.d. over an ensemble of n bundles. With myosin II, only 46 out of the 59 bundles were long enough ($L>11$ μm) to show saturation of the tangent angle; the value of ψ_{MAX} was thus determined with these $n=46$ bundles. To compare the mean values obtained with the two motor types, we used two-tailed unpaired Student's t-tests with Welch's correction. The asterisks correspond to p values with *$p<0.05$, **$p<0.01$, ***$p<0.001$ and ****$p<0.0001$, whereas 'n.s.' ($p>0.05$) indicates non-significant differences.

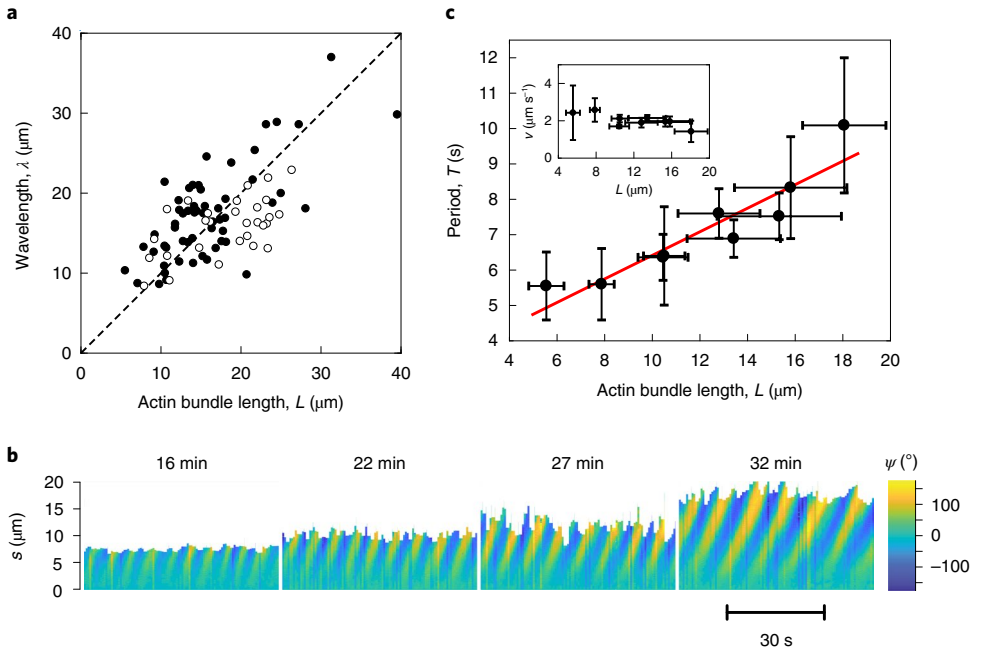

Fig. 3 | Beating properties as a function of actin bundle length. a, Wavelength λ of actin-bending waves as a function of actin bundle length L for beating bundles driven by myosin II (black disks) or myosin V (white disks). The dashed line has a slope of unity. **b**, Colour plots of tangent angle ψ to an actin bundle's centre line as a function of arc length s and time t. Four successive recordings were obtained with the same actin bundle. Each recording started at different times with respect to the initiation of actin polymerization, as indicated on the top of each panel. Here actin beating was driven by myosin II and displayed stationary properties over the 1-min duration of each recording. **c**, Period T of tangent angle oscillations and velocity v of actin-bending waves (inset) as a function of actin bundle length L. The red line represents a linear fit with slope 0.33 ± 0.12 s μm^{-1} (95% confidence bounds) to the relationship $T(L)$. Error bars for L and T are s.d. values over the duration of each recording. Error bars for v are 95% confidence bounds to the linear fits of the relationship $\phi(s)$ between the phase of tangent angle oscillations and the arc length. Same actin bundle as in **b**.

Supplementary Video 10). By repeating these measurements over an ensemble of beating bundles, we observed that the myosin waves were produced at precisely twice the frequency of actin-bending waves, corresponding to periods of 20.7 ± 6.0 and 41.1 ± 12.4 s ($n=10$), respectively. The velocity $v_V^{myo}=0.7\pm0.2$ μm s^{-1} ($n=17$) of the myosin waves was 1.4–3.0 times the velocity reported for myosin V transport in in vitro gliding or bead assays[31–33] but comparable to that of in vitro processive movements of single myosin V molecules on actin filaments[34] and of the transport velocities measured inside cells[35]. The myosin density peak may travel towards the bundle's tip because the attached motors move progressively along the actin filaments or because the motors continuously bind to the front and unbind from the rear of a travelling motor collection, or both. Because myosin recruitment did not happen at the very base of the actin bundle but at a more apical position, the velocity of the myosin waves was, on average, only 1.7-fold larger than the velocity $v_V^{act}=0.42\pm0.15$ μm s^{-1} ($n=17$) of the corresponding actin-bending waves.

Superimposing the myosin density profiles (Fig. 4a) and actin curvature profiles (Fig. 4b) provides the envelopes of the two interrelated waves. The amplitude of the actin bundle curvature wave increased smoothly as the wave travelled from the bundle's base towards its tip before saturating. In contrast, the corresponding myosin density increased abruptly at the position $s^*=6.9\pm1.8$ μm where the actin curvature reached the threshold value $C^*=0.65\pm0.09$ μm^{-1}, as measured over an ensemble of $n=14$ beating bundles. This observation suggests that myosin recruitment from the bulk to the actin filament bundle depends on the

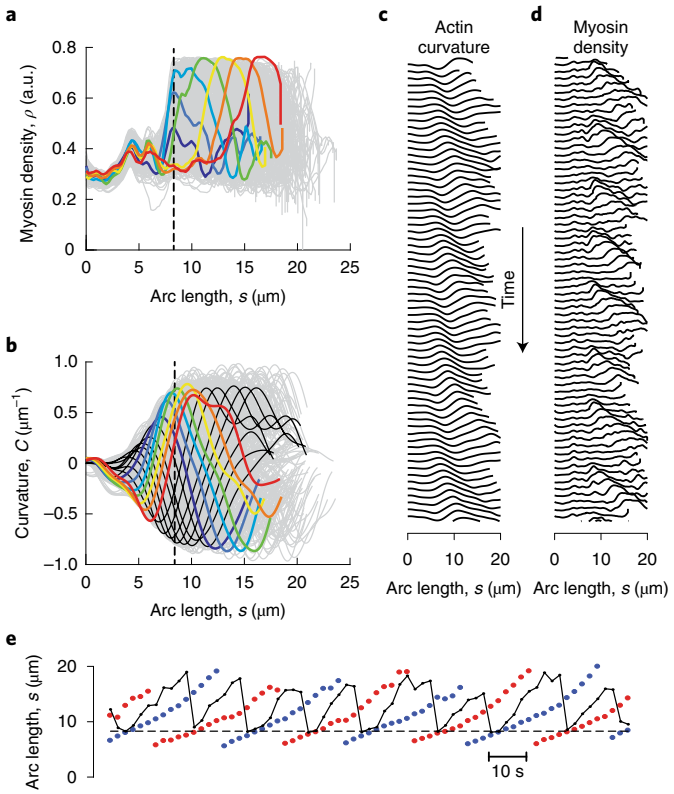

Fig. 4 | Interplay between myosin V density and actin curvature waves. **a**, Myosin density profiles (arbitrary units (a.u.)) during one period of a myosin density wave (here it is 15.3 s). The order of the line colours, from dark blue to red, indicates time progression over one period of the myosin density waves with a 2-s time interval. **b**, Actin curvature profiles during one period of bending oscillation (here it is 30.6 s). The actin curvature profiles associated with the myosin density profiles (shown in **a**) are indicated using the same line colours. The grey areas in **a** and **b** were obtained by superimposing the myosin density and actin curvature profiles, respectively, over 22 periods of bending oscillations, revealing the envelopes of the corresponding waves. **c**, Kymograph of actin curvature profiles (a.u.). **d**, Kymograph of myosin density profiles (a.u.). In **a**–**d**, there is a 2-s interval between the two successive profiles. **e**, Arc length as a function of time for the points along the bundle's centre line at which the actin curvature is maximum (red disks), minimum (blue disks) and at which the myosin density peaks (black dots and line). For this bundle, the arc length $s^* = 8.3 \pm 0.9\,\mu$m at which the myosin density increases abruptly, corresponding to myosin recruitment in the actin bundle at the threshold curvature $C^* = 0.63 \pm 0.09\,\mu\text{m}^{-1}$, is marked by dashed lines in **a**, **b** and **e**. The slope of the rising phase in sawtooth oscillations of myosin density provided a velocity of $v_V^{myo} = 0.7 \pm 0.2\,\mu\text{m}\,\text{s}^{-1}$. Here the s.d. values from the mean were calculated over 29 periods of myosin density waves.

magnitude of the bundle's local curvature. At the time of recruitment, the myosin peak was localized near a position of the maximum absolute curvature in the actin bundle (Fig. 4e, Extended Data Fig. 6 and Supplementary Videos 7 and 10). At later times, although the waves continued travelling towards the bundle's tip, both the actin curvature and the myosin density remained at saturated values (Fig. 4a,b). However, because myosin density waves travelled faster than actin curvature waves, the myosin peak did not co-localize with the position of the maximum absolute actin curvature but was positioned farther towards the bundle's tip (Fig. 4c–e and Extended Data Fig. 6). We note that the ratio of the s.d. to the mean for the threshold curvature C^* was small—only 14%. Over the same ensemble of beating bundles, the bundle width $W^* = 0.66 \pm 0.09\,\mu$m ($n = 14$) at the position s^* of myosin recruitment also showed small variations, indicating that the beating bundles were similar in our experiments.

Thus, the visualization of motors revealed a nonlinear self-organization process. Bending waves of the actin filament bundles are associated with myosin density waves generated at twice the frequency of bending oscillations. In the following, we present a theory showing how the wave-like beating of an active filament bundle may emerge from the dynamic interplay between bending of the bundle and curvature-dependent motor binding to the filaments.

Physical description of self-organized beating. To account for our experimental observations, we built a coarse-grained theory of an active filament bundle that generates wave-like beating through a dynamic instability (Supplementary Information). The theory keeps track of a minimum set of mesoscopic variables as a function of time t and arc length s: the angle $\psi(t,s)$ between the tangent to the centre line of the bundle and the vertical axis, which describes the shape of the bundle, the total lineic density $\rho(t,s)$ of bound motors and the algebraic lineic density $\rho_a(t,s)$ of active motor crosslinks that generate internal torques within the bundle. The dynamic equations for these variables are obtained from symmetry arguments and conservation laws.

The active torques that drive beating are generated by motors that form transient crosslinks between filaments. A motor-mediated crosslink between a filament pair can produce a clockwise or anticlockwise torque, depending on whether the motor advances on one or the other filament of the pair. We denote the corresponding lineic densities of active crosslinks in a cross section of the filament bundle by $\rho_+(t,s)$ and $\rho_-(t,s)$ and we define the algebraic lineic density $\rho_a(t,s) = (\rho_+ - \rho_-)/N(s)$ of active crosslinks per filament. The bundle is a heterogeneous structure comprising aligned polar filaments of different lengths. The number $N(s)$ of filaments in a cross section decreases exponentially with arc length s. The net active torque at arc length s is given by $N(s)A_0\rho_a(t,s)$, where A_0 is the magnitude of the torque produced by an active crosslink. Here we propose that the active torque per filament and per unit length increases at a rate of $A_0 k_a C$ proportional to bundle curvature $C = \partial_s\psi$ and relaxes at rate k_d. A linear relation is expected if the radius of curvature of the bundle is larger than the diameter of the bundle's cross section. The parameter k_a characterizes the curvature dependence of the active torque. This coupling generates positive feedback between the torque and curvature. Because of the delay due to the binding and unbinding kinetics of active crosslinks, the active filament bundle can undergo an oscillatory instability—a Hopf bifurcation—beyond a critical value Ω_c of the control parameter $\Omega = A_0 k_a / k_d$, resulting in the emergence of wave-like beating.

Beating of the filament bundle is associated with a density wave of bound motors $\rho(t,s)$, with abrupt motor recruitment beyond a threshold value of bundle curvature $C = C^*$. Because recruitment happens near the base of the filament bundle and is followed by the propagation of a motor density peak of constant amplitude, we propose that $C^* = C_0/N(s)$ is inversely related to the local number of filaments: the larger the local number of filaments, the easier it is to recruit motors as a result of bundle bending at this position. The mechanosensitivity of motor binding is, thus, a cooperative behaviour of the filament bundle. Finally, we consider the simple limit in which dissipation is dominated by internal shear friction, with a friction coefficient per filament ξ_0, and that viscous drag by the surrounding fluid only provides a small contribution (section 6 in the Supplementary Information). This limit is valid for sufficiently short bundles. In this regime of high internal friction, the dynamic equation for $\psi(t,s)$ depends only weakly on the number of filaments in the bundle.

At the Hopf bifurcation ($\Omega = \Omega_c$), wave-like beating emerges at frequency $\omega_c \simeq k_d \sqrt{\frac{2\pi^2}{L^2}\frac{\kappa_0}{\xi_0 k_d} + 1}$, where L is the bundle length and κ_0 is the bending rigidity per filament. For the parameter

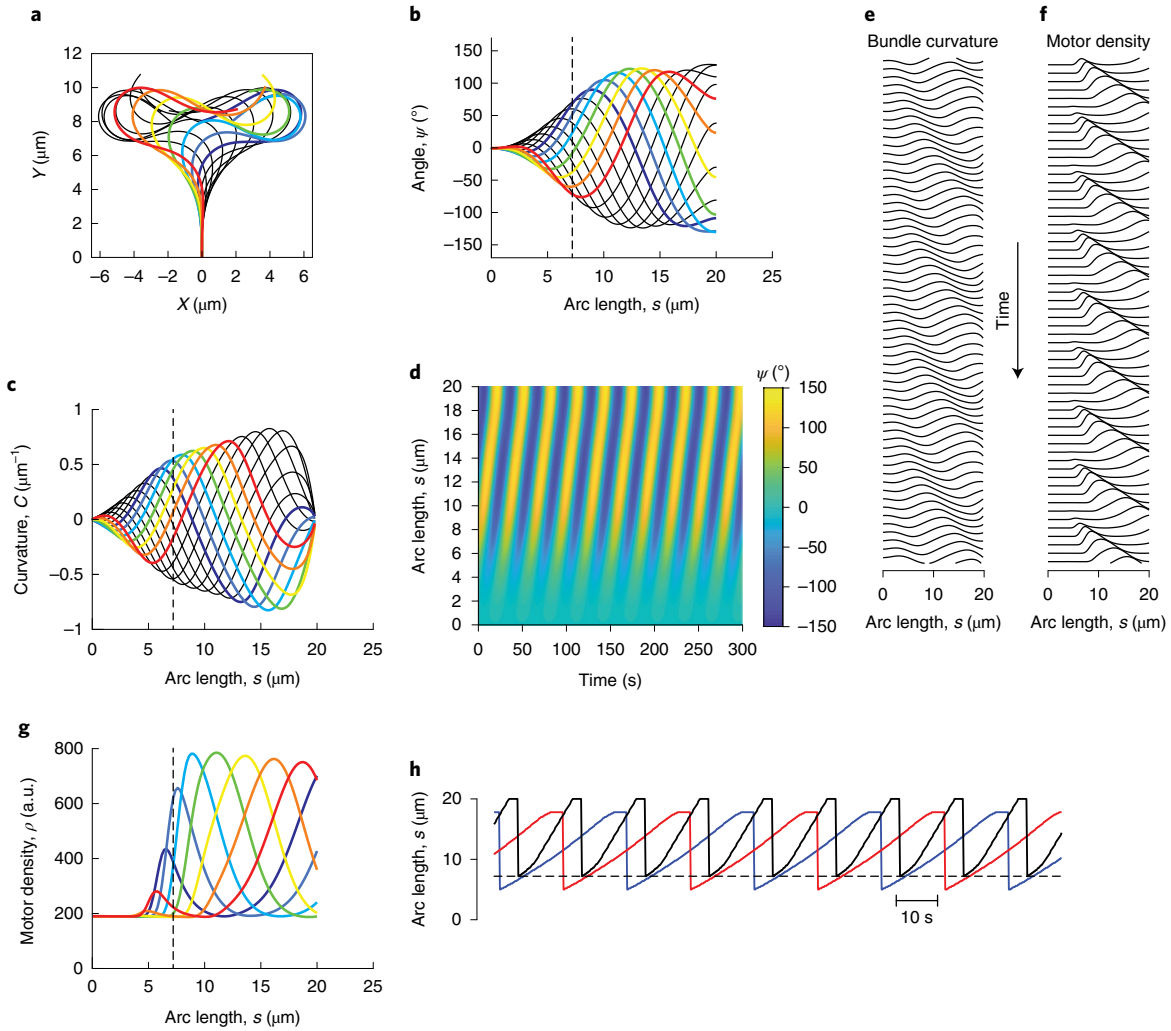

Fig. 5 | Wave-like beating in a model of an active filament bundle. a, Wave-like beating pattern of the bundle's centre line. **b**, Tangent angle $\psi(t,s)$ to the centre line shown in **a** as a function of arc length s at successive values of time t over one period of bending oscillation. **c**, Curvature profiles $C(t,s)=\partial_s\psi$ resulting from the tangent angle profiles $\psi(t,s)$ shown in **b**. **d**, Colour plot of the tangent angle $\psi(t,s)$, revealing bending waves travelling from the base towards the tip of the bundle at a velocity of 0.56 μm s^{-1} and beating with a period of 30.6 s. The corresponding curvature waves $C(t,s)$ are associated with motor density waves $\rho(t,s)$, both of which are shown as kymographs in **e** and **f**, respectively. **g**, Profiles $\rho(t,s)$ of the total density of bound motors. **h**, Arc length as a function of time of the points along the bundle's centre line at which the bundle curvature is the maximum (red line), minimum (blue line) and at which the motor density peaks (black solid line). The motor density peak travels at a velocity of 1.1 μm s^{-1}. There is a 2.2 s interval between two successive profiles in **a**–**c** and **e**–**g**. The arc length $s=7.2$ μm at which the motor density increases abruptly, corresponding to motor recruited in the actin bundle, is marked by a dashed line in **b**, **c**, **g** and **h**. In **a**–**c** and **g**, the order of the line colours, from dark blue to red, indicates time progression over one period of the motor density waves with a 2.2 s time interval. These results are numerical solutions of the equations and parameter values listed in the Supplementary Information.

values listed in Supplementary Tables 1 and 2, our numerical solutions show bending waves travelling from the base to the tip of the bundle at a nearly uniform velocity over most of the bundle's length and beating patterns with characteristic figure-of-eight patterns (Fig. 5a–d). Curvature waves (Fig. 5e) are associated with motor density waves (Fig. 5f and Supplementary Video 11). The motors bind to the filaments near the base of the bundle at twice the frequency of the bending oscillations. Motor binding corresponds to the sudden appearance of a localized motor density peak $\rho(t,s)$ where and when the bundle reaches a threshold curvature (Fig. 5g). The motor density wave then travels with a nearly constant magnitude towards the bundle's tip, with a velocity larger than that of the curvature wave (Fig. 5h). As in experiments, the myosin density peak remains within a restricted region of the X–Y plane, near the centre of the figure-of-eight pattern in the beat pattern (Extended Data Figs. 5b and 7).

Overall, a simple model based on nonlinear curvature control of motor binding, on curvature control of active torque generation and on high internal shear friction captures the key features of the complex interplay between actin-bending waves and myosin density waves observed in experiments.

Discussion

Using a bottom-up approach based on a minimal active molecular system, we have demonstrated here that wave-like beating emerges robustly in polar bundles of actin filaments and myosin motors. In the presence of myosin motor dimers added in the bulk, growing actin filaments self-organize into beating bundles. Beating takes the form of bending waves with shapes resembling those observed in eukaryotic cilia and flagella, as well as in reconstituted kinesin–microtubule systems[19], despite the different families of filaments and motors at work. Thus, our finding provides further evidence

that the emergence of wave-like oscillations is a generic feature of motor filament systems, irrespective of the molecular details, providing experimental support for the general theories of this form of active matter[11,21].

Our assay is based on protein micropatterning, which allows to control the self-assembly of actin filament bundles and their spatial organization. In addition, the visualization of motors as the actin bundle is beating revealed that the actin-bending waves are associated with myosin density waves: the motor density increased abruptly beyond a threshold value of the bundle curvature before travelling towards the tip of the actin bundle (Fig. 4). These observations suggest that the filament bundle shape regulates myosin attachment to actin, which could provide a feedback mechanism between motor activity and filament bending[8,9]. This mechanism contrasts with shape-dependent detachment as the basis of a dynamic instability that can give rise to spontaneous oscillations[5,36,37], although the two mechanisms are not mutually exclusive.

How could the motors' affinity for the filaments depend on the filament bundle shape? There is a growing bulk of evidence showing that actin filaments are endowed with conformational plasticity[38–40], that bending can evoke structural transitions in actin filaments[41] and that protein binding can stabilize a specific conformational state of actin, as shown for myosin V (ref. [42]) in direct relevance to our work as well as for other proteins[43,44]. Strong binding of myosin II has also been shown to reduce the helical angle of F-actin, elongating the filament[45]. Actin filaments, therefore, can act as mechanosensors because an applied force that alters their conformation should also affect their affinity for actin-binding proteins[40,46–49]. Myosin motor molecules are actin-binding proteins that can actively exert physical stresses on the filaments by converting energy from a biochemical fuel (here adenosine triphosphate; ATP) into mechanical work. Tension of only a few piconewtons—a magnitude comparable to that exerted by a single myosin motor[30]—appears to be strong enough to distort the actin filament structure[50]. Thus, the actin filament does not simply operate as a passive cable to which proteins can bind but can provide feedback on protein binding and activity.

We have shown, on general theoretical grounds, that a positive feedback between curvature and active torque generation by the motors is sufficient for the emergence of self-organized bending waves in a polar filament bundle (Fig. 5 and Supplementary Information). This feedback mechanism is the simplest allowed by symmetry to linear order. By introducing nonlinearities that account for the observed curvature dependence of myosin binding, the theory quantitatively reproduces the main features of the experimental curvature and motor density waves (Figs. 4 and 5 and Supplementary Videos 7, 8 and 11). Curvature control of motor activity had earlier been proposed to mediate motor coordination in eukaryotic flagella[8,9], particularly to account for waveforms in isolated *Chlamydomonas* axonemes[12,16]. In our work, curvature control is described as an emergent behaviour at a coarse-grained level based on symmetry arguments. As in studies of the flagellar beat that also invoke such feedback, we do not address here the detailed molecular mechanism by which the motors sense the curvature of the filament bundle. This question remains a key open challenge in all these systems in view of the small estimated strains resulting from curvature changes in the filaments[12]. In addition, we cannot preclude that the regulation of motor activity in our assay also involves other phenomena. In particular, in the case of eukaryotic flagella, regulation by shear forces resulting from interfilament sliding[4,5,11] or by transverse forces from variations in the interfilament lateral distance—a mechanism known as 'geometric clutch'[2]—have been invoked. Such concepts could also be relevant to motor regulation in the assay studied here. Finally, future experiments ought to characterize the nature of individual motor motion within the myosin density waves, test how curvature control of myosin binding depends on the number of filaments in the bundle, and quantitatively determine the relative importance of internal and external contributions to friction as a function of the bundle architecture.

In conclusion, our in vitro work with a minimal actomyosin system shows that the emergence of self-organized bending waves is a generic feature of motor filament systems. We shed light on the dynamic interplay between myosin binding, myosin activity and filament bundle shape, opening an avenue for understanding the self-organization of this type of active matter.

Online content

Any methods, additional references, Nature Research reporting summaries, source data, extended data, supplementary information, acknowledgements, peer review information; details of author contributions and competing interests; and statements of data and code availability are available at https://doi.org/10.1038/s41567-022-01688-8.

Received: 12 June 2021; Accepted: 23 June 2022;
Published online: 08 August 2022

References

1. Nicastro, D. The molecular architecture of axonemes revealed by cryoelectron tomography. *Science* **313**, 944–948 (2006).
2. Lindemann, C. B. & Lesich, K. A. Flagellar and ciliary beating: the proven and the possible. *J. Cell Sci.* **123**, 519–528 (2010).
3. Pazour, G. J., Agrin, N., Leszyk, J. & Witman, G. B. Proteomic analysis of a eukaryotic cilium. *J. Cell Biol.* **170**, 103–113 (2005).
4. Brokaw, C. J. Molecular mechanism for oscillation in flagella and muscle. *Proc. Natl Acad. Sci. USA* **72**, 3102–3106 (1975).
5. Riedel-Kruse, I. H., Hilfinger, A., Howard, J. & Julicher, F. How molecular motors shape the flagellar beat. *HFSP J.* **1**, 192–208 (2007).
6. Machin, K. E. Wave propagation along flagella. *J. Exp. Biol.* **35**, 796–806 (1958).
7. Brokaw, C. J. Computer simulation of flagellar movement VIII: coordination of dynein by local curvature control can generate helical bending waves. *Cell Motil. Cytoskeleton* **53**, 103–124 (2002).
8. Brokaw, C. & Rintala, D. Computer simulation of flagellar movement. III. Models incorporating cross-bridge kinetics. *J. Mechanochem. Cell* **3**, 77–86 (1975).
9. Hines, M. & Blum, J. J. Bend propagation in flagella. I. Derivation of equations of motion and their simulation. *Biophys. J.* **23**, 41–57 (1978).
10. Lindemann, C. B. A 'geometric clutch' hypothesis to explain oscillations of the axoneme of cilia and flagella. *J. Theor. Biol.* **168**, 175–189 (1994).
11. Camalet, S. & Jülicher, F. Generic aspects of axonemal beating. *New J. Phys.* **2**, 24 (2000).
12. Sartori, P., Geyer, V. F., Scholich, A., Julicher, F. & Howard, J. Dynamic curvature regulation accounts for the symmetric and asymmetric beats of *Chlamydomonas* flagella. *eLife* **5**, e13258 (2016).
13. Oriola, D., Gadêlha, H. & Casademunt, J. Nonlinear amplitude dynamics in flagellar beating. *R. Soc. Open Sci.* **4**, 160698 (2017).
14. Mondal, D., Adhikari, R. & Sharma, P. Internal friction controls active ciliary oscillations near the instability threshold. *Sci. Adv.* **6**, eabb0503 (2020).
15. Nandagiri, A. et al. Flagellar energetics from high-resolution imaging of beating patterns in tethered mouse sperm. *eLife* **10**, e62524 (2021).
16. Geyer, V. F., Howard, J. & Sartori, P. Ciliary beating patterns map onto a low-dimensional behavioural space. *Nat. Phys.* **18**, 332–337 (2022).
17. Bourdieu, L. et al. Spiral defects in motility assays: a measure of motor protein force. *Phys. Rev. Lett.* **75**, 176–179 (1995).
18. Placais, P. Y., Balland, M., Guerin, T., Joanny, J. F. & Martin, P. Spontaneous oscillations of a minimal actomyosin system under elastic loading. *Phys. Rev. Lett.* **103**, 158102 (2009).
19. Sanchez, T., Welch, D., Nicastro, D. & Dogic, Z. Cilia-like beating of active microtubule bundles. *Science* **333**, 456–459 (2011).
20. Jülicher, F. & Prost, J. Spontaneous oscillations of collective molecular motors. *Phys. Rev. Lett.* **78**, 4510–4513 (1997).
21. Guerin, T., Prost, J., Martin, P. & Joanny, J. F. Coordination and collective properties of molecular motors: theory. *Curr. Opin. Cell Biol.* **22**, 14–20 (2010).
22. Reymann, A. C. et al. Nucleation geometry governs ordered actin networks structures. *Nat. Mater.* **9**, 827–832 (2010).
23. Reymann, A. C., Guerin, C., Thery, M., Blanchoin, L. & Boujemaa-Paterski, R. Geometrical control of actin assembly and contractility. *Methods Cell. Biol.* **120**, 19–38 (2014).
24. Richard, M. et al. Active cargo positioning in antiparallel transport networks. *Proc. Natl Acad. Sci. USA* **116**, 14835–14842 (2019).

25. Letort, G. et al. Geometrical and mechanical properties control actin filament organization. *PLoS Comput. Biol.* **11**, e1004245 (2015).
26. Köhler, S., Lieleg, O. & Bausch, A. R. Rheological characterization of the bundling transition in F-actin solutions induced by methylcellulose. *PLoS ONE* **3**, e2736 (2008).
27. Gray, J. The movement of the spermatozoa of the bull. *J. Exp. Biol.* **35**, 96–108 (1958).
28. Rikmenspoel, R. Movements and active moments of bull sperm flagella as a function of temperature and viscosity. *J. Exp. Biol.* **108**, 205–230 (1984).
29. De La Cruz, E. M. & Ostap, E. M. Relating biochemistry and function in the myosin superfamily. *Curr. Opin. Cell Biol.* **16**, 61–67 (2004).
30. Howard, J. *Mechanics of Motor Proteins and the Cytoskeleton* (Sinauer Associates, 2001).
31. Mehta, A. D. et al. Myosin-V is a processive actin-based motor. *Nature* **400**, 590–593 (1999).
32. Rief, M. et al. Myosin-V stepping kinetics: a molecular model for processivity. *Proc. Natl Acad. Sci. USA* **97**, 9482–9486 (2000).
33. Clemen, A. E. et al. Force-dependent stepping kinetics of myosin-V. *Biophys. J.* **88**, 4402–4410 (2005).
34. Sakamoto, T. et al. Neck length and processivity of myosin V. *J. Biol. Chem.* **278**, 29201–29207 (2003).
35. Pierobon, P. et al. Velocity, processivity, and individual steps of single myosin V molecules in live cells. *Biophys. J.* **96**, 4268–4275 (2009).
36. Howard, J. Mechanical signaling in networks of motor and cytoskeletal proteins. *Annu. Rev. Biophys.* **38**, 217–234 (2009).
37. Ma, R., Klindt, G. S., Riedel-Kruse, I. H., Jülicher, F. & Friedrich, B. M. Active phase and amplitude fluctuations of flagellar beating. *Phys. Rev. Lett.* **113**, 048101 (2014).
38. Egelman, E. H., Francis, N. & DeRosier, D. J. F-actin is a helix with a random variable twist. *Nature* **298**, 131–135 (1982).
39. Galkin, V. E., Orlova, A., Schroder, G. F. & Egelman, E. H. Structural polymorphism in F-actin. *Nat. Struct. Mol. Biol.* **17**, 1318–1323 (2010).
40. Galkin, V. E., Orlova, A. & Egelman, E. H. Actin filaments as tension sensors. *Curr. Biol.* **22**, R96–R101 (2012).
41. Reynolds, M. J., Hachicho, C., Carl, A. G., Gong, R. & Alushin, G. M. Actin nucleotide state modulates the F-actin structural landscape evoked by bending forces. http://biorxiv.org/lookup/doi/10.1101/2022.06.02.494606 (2022).
42. Kozuka, J., Yokota, H., Arai, Y., Ishii, Y. & Yanagida, T. Dynamic polymorphism of single actin molecules in the actin filament. *Nat. Chem. Biol.* **2**, 83–86 (2006).
43. McGough, A., Pope, B., Chiu, W. & Weeds, A. Cofilin changes the twist of F-actin: implications for actin filament dynamics and cellular function. *J. Cell Biol.* **138**, 771–781 (1997).
44. Risca, V. I. et al. Actin filament curvature biases branching direction. *Proc. Natl Acad. Sci. USA* **109**, 2913–2918 (2012).
45. Tsaturyan, A. K. et al. Strong binding of myosin heads stretches and twists the actin helix. *Biophys. J.* **88**, 1902–1910 (2005).
46. Jegou, A. & Romet-Lemonne, G. The many implications of actin filament helicity. *Semin. Cell Dev. Biol.* **102**, 65–72 (2020).
47. Mei, L. et al. Molecular mechanism for direct actin force-sensing by α-catenin. *eLife* **9**, e62514 (2020).
48. Winkelman, J. D., Anderson, C. A., Suarez, C., Kovar, D. R. & Gardel, M. L. Evolutionarily diverse LIM domain-containing proteins bind stressed actin filaments through a conserved mechanism. *Proc. Natl Acad. Sci. USA* **117**, 25532–25542 (2020).
49. Sun, X. et al. Mechanosensing through direct binding of tensed F-actin by LIM domains. *Dev. Cell* **55**, 468–482 (2020).
50. Shimozawa, T. & Ishiwata, S. Mechanical distortion of single actin filaments induced by external force: detection by fluorescence imaging. *Biophys. J.* **96**, 1036–1044 (2009).

Methods

Micropatterning of an actin nucleation-promoting factor. The fusion protein His–pWA–streptavidin (also called S-pVCA) was produced and characterized following a published protocol[51]; the histidine (His) tag was used for purification purposes and streptavidin had no function in this work. The protein pWA comprises the C-terminal domain from the Wiskott–Aldrich-syndrome protein/Scar protein, a ubiquitous family of proteins that initiate actin polymerization on a pre-existing actin filament in the presence of the Arp2/3 complex and actin monomers. Micropatterning of this actin nucleation-promoting factor was performed as previously described[22–24]. In short, glass coverslips were oxidized for 2 min with an oxygen plasma and then passivated by incubating them with 0.1 mg ml^{-1} poly(L-lysine)-*graft*-poly(ethylene glycol) (Jenkem Technology) in 10 mM 4-(2-hydroxyethyl)−1-piperazineethanesulfonic acid at pH 7.4 for 1 h. The passivated surfaces were exposed to deep ultraviolet light (wavelength, 180 nm; UVO Cleaner Unit 342; Jelight Company) for 5 min through a transparent micropattern printed on a chromium synthetic quartz photomask (Toppan Photomasks). The coverslips were then incubated with 1 µM His–pWA–streptavidin in a buffer containing 50 mM KCl, 1 mM $MgCl_2$, 1 mM ethylene glycol-bis(β-aminoethyl ether)-*N*,*N*,*N*′,*N*′-tetraacetic acid and 10 mM imidazole–HCl at pH 7.8 for 10 min. In our experiments, the pattern was typically composed of 9-µm-diameter disks.

Actin polymerization in the presence of myosin motors. Actin polymerization from the surface micropatterns of the nucleation-promoting factor His–pWA–streptavidin was induced in a solution containing 2 µM globular actin (Tebu-Bio), 8 µM profilin (produced as described elsewhere[51]), 80 nM Arp2/3 complex (Tebu-Bio) and myosin molecular motors. We used one of the following two types of myosin molecule. First, double-headed heavy meromyosin II—here simply called myosin II, purified from the rabbit pectoral muscle according to a published protocol[52]—was provided by the group of Matthias Rief (Technische Universität München) and used at a typical concentration of 500 nM (range, 250–1,500 nM). Second, recombinant double-headed myosin Va missing the C-terminal globular tail and fused to the GFP—here called myosin V—was produced as described elsewhere[53] and used at a concentration of 50 nM. The buffer of the actomyosin polymerization solution was composed of 10.0 mM imidazole–HCl (pH 7.8), 50.0 mM KCl, 1.0 mM $MgCl_2$, 4.2 mM disodium adenosine triphosphate, 56.0 mM dithiothreitol, 0.1 mg ml^{-1} glucose, 42.0 nM catalase, 0.6 mM glucose oxidase and 0.3% (w/v) methylcellulose. Using an Ubbelohde viscometer (type Ib; SI Analytics), we measured a viscosity of 15 mPa s for this solution at 27 °C. To visualize the actin filaments, 10% of the monomers were labelled with a fluorophore (Alexa 568; Life Technologies). A thermostat-controlled chamber ensured that the experiments were performed at a constant temperature of 27 °C.

Microscopic observations. Our samples were observed through a 60× objective (numerical aperture, 1.4) of a spinning-disk confocal microscope (ECLIPSE 80i; Nikon). Time-lapse videos were recorded with an electron-multiplying charge-coupled device camera (Ultra 897 iXon) at time intervals ranging from 0.2 to 2.0 s. Time-lapse recordings could start as early as 5 min after the injection of the polymerization mix into the flow chamber and last up to 1 h.

Image analysis. We used the ridge-detection plugin[54] of the image-processing software ImageJ (NIH) to automatically track the centre line of the actin filament bundles. The bundles appeared as bright curvilinear objects on a dark background as a result of actin fluorescence labelling (Fig. 1a). Regions of interest with well-separated bundles were first selected. Only the beating part of the bundle was selected. A region of interest could encompass most of the bundle's length, from the border of the actin nucleation area to the bundle's tip (Supplementary Video 1 and Extended Data Fig. 1d (white box)), or be positioned some distance away from the nucleation area (Supplementary Videos 3 and 8 and Extended Data Fig. 1f (white box)). If necessary, a rotation was applied on the selected regions to vertically orient the base of the target bundle. Neighbouring bundles were deleted from the greyscale images to ensure that the tracking procedure did not yield parasite sets of coordinates. The output of the ridge-detection plugin was a stack of images, each showing the bundle's centre line as a black line on a white background at a given time point. In each image, we then extracted and ordered the (X, Y) coordinates of the detected line. Each of these coordinates was smoothed using a moving average with a span of five points, before computing the arc length s along the bundle's centre line. After a linear interpolation of the relations $(X(s), Y(s))$ with an arc-length increment of 0.01 µm, corresponding to about 1/25th of the pixel size, we parametrized the shape of the centre line by computing, at each point of the line, the tangent angle $\psi(t, s)$ relative to the vertical axis (Y axis). At each time t, the relation $\psi(s)$ was then smoothed using a Gaussian filter with s.d. of 100 points, corresponding to a distance of 1 µm or about 1/20th of the wavelength of the bending waves, before computing the local curvature $\psi'(t, s) = \mathrm{d}\psi/\mathrm{d}s$. The base of the bundle was located at $s = 0$ and its tip at $s = L$, where the bundle's length $L(t)$ slowly increased over time as a result of actin polymerization. The amplitude of tangent angle oscillations (Fig. 1d) was defined as $\psi_0(s) = \sqrt{2\langle(\psi(t,s) - \langle\psi(t,s)\rangle)^2\rangle}$, where $\langle\cdot\rangle$ denotes the time average over the duration of the recording. Their period T and phase $\phi(s)$ were obtained from the frequency $(1/T)$ and phase at the peak of the Fourier transform, namely, $\tilde{\psi}(\omega, s) = \int \psi(t, s)\mathrm{e}^{-i\omega t}\mathrm{d}t$. We then calculated the local wavelength $\lambda(s) = -2\pi/\phi'$ and velocity $v = \lambda/T$ of the actin-bending waves. Myosin density profiles $\rho(t, s)$ were obtained by computing—as a function of time—the intensity of the myosin fluorescence signal along the actin bundle's centre line. The velocity of the myosin density wave was obtained by tracking the arc length of the myosin density peak along the bundle as a function of time (Fig. 4e, black line). Data analysis was performed using custom software written in MATLAB (release R2018a; MathWorks).

Statistical testing. Unless otherwise indicated, all the results are quoted as mean ± s.d. over an ensemble of n actin filament bundles. Statistical significance of the difference between the means over two data ensembles—in practice, the data obtained with beating bundles driven with myosin II and myosin V—was assessed using a two-tailed Student's t-test with Welch's correction. Correlations were assessed by computing a Pearson's correlation coefficient and its p value.

Reporting summary. Further information on research design is available in the Nature Research Reporting Summary linked to this article.

Data availability

Source data are available for this paper. All other data that support the plots within this paper and other findings of this study are available from the corresponding author upon reasonable request.

References

51. Carvalho, K. et al. Actin polymerization or myosin contraction: two ways to build up cortical tension for symmetry breaking. *Philos. Trans. R. Soc. B* **368**, 20130005 (2013).
52. Margossian, S. S. & Lowey, S. Preparation of myosin and its subfragments from rabbit skeletal muscle. *Methods Enzym.* **85**, 55–71 (1982).
53. Snyder, G. E., Sakamoto, T., Hammer, J. A., Sellers, J. R. & Selvin, P. R. Nanometer localization of single green fluorescent proteins: evidence that myosin V walks hand-over-hand via telemark configuration. *Biophys. J.* **87**, 1776–1783 (2004).
54. Steger, C. An unbiased detector of curvilinear structures. *IEEE Trans. Pattern Anal. Mach. Intell.* **20**, 113–125 (1998).

Acknowledgements

We are indebted to M. Rief for providing the heavy meromyosin II molecules. We thank the Cell and Tissue Imaging core facility (PICT-IBiSA) of the Institut Curie, a member of the French National Research Infrastructure France-BioImaging (ANR10-INBS-04). We thank J. Manzi for protein purification and characterization; F. Di Federico for the genetic construct of His–pWA–streptavidin; J.-Y. Tinevez, A. Allard and I. Bonnet for help with MATLAB programming; H. Ennomani and C. Guérin for help with actin micropatterning; and J. Plastino and C. Sykes for fruitful discussions. This work was supported by the French National Agency for Research (ANR-12-BSV5 0014; P.M. and L.B. and ANR-21-CE30-0057; PM and FJ), Labex Cell(n)Scale ANR-11-LABX-0038 and ANR-10-IDEX-001-02, United States National Institutes of Health Grant R35-GM135656 (E.M.D.L.C.) and European Research Council (741773 (AAA); L.B.).

Author contributions

M.P. and M.M. contributed equally to the work. M.P., M.M., M.R., A.C., J.-F.J., F.J., L.B. and P.M. designed and performed the research and analysed the data. Y.T., W.C., E.M.D.L.C. and J.R.S. provided the new reagents. M.P., M.M., J.-F.J, F.J., L.B. and P.M. wrote the article.

Competing interests

The authors declare no competing interests.

Additional information

Extended data is available for this paper at https://doi.org/10.1038/s41567-022-01688-8.

Supplementary information The online version contains supplementary material available at https://doi.org/10.1038/s41567-022-01688-8.

Correspondence and requests for materials should be addressed to Pascal Martin.

Peer review information *Nature Physics* thanks Hermes Bloomfield-Gadêlha and the other, anonymous, reviewer(s) for their contribution to the peer review of this work.

Reprints and permissions information is available at www.nature.com/reprints.

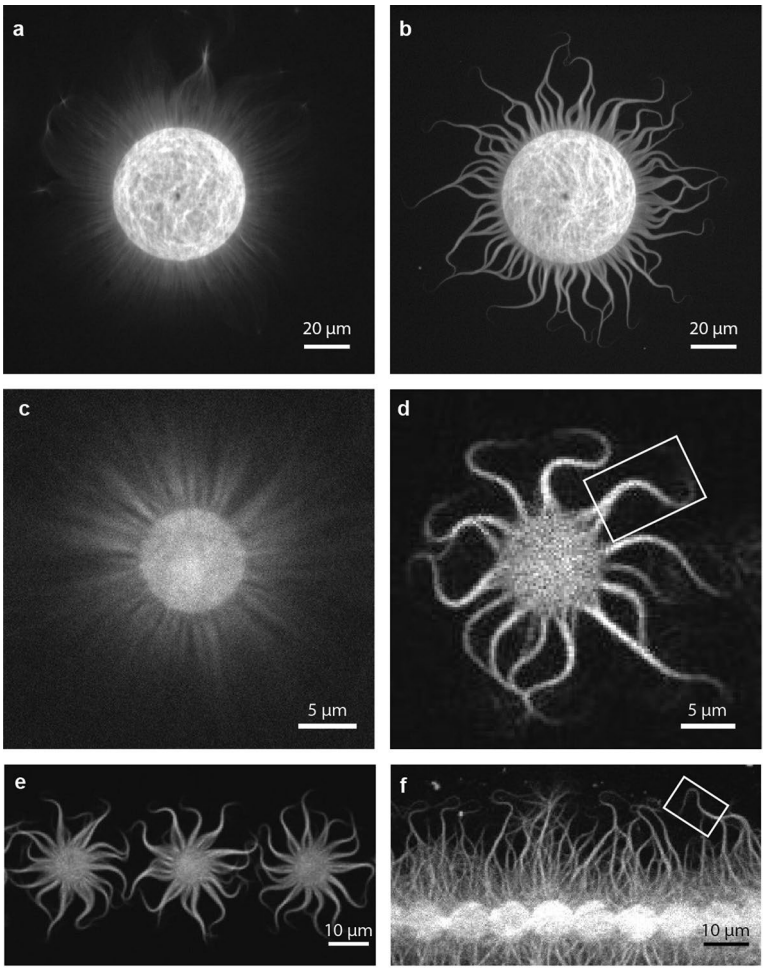

Extended Data Fig. 1 | Actin micropatterns with or without myosin motors. a, Radial network of actin filaments that have grown away from the border of a single 60-µm nucleation disk of actin polymerization (no motors). There is a branched filament network on the disk surface. **b**, With the same disk of actin nucleation as in **a**, polymerization in the presence of myosin II motors added in bulk results in the formation of actin filament bundles that are curved near their tips. **c** and **d**, Same as in **a** and **b**, respectively, but with a smaller, 9-µm nucleation disk. **e**, Similar actin pattern as that shown in **d** but bundling and beating are here driven by myosin V. **f**, A line of contiguous 9-µm disks results in a more complex arrangement of actin filament bundles. Although the bundles are static in their basal half, myosin-V driven beating is observed in a region that spans about 20 µm from the bundles' tips. Beating of the bundles seen in **d**, **e** and **f** can be visualized in Supplementary Videos 1, 2, and 3, respectively. The beating properties of the bundle in the box of **d** and **f** are analysed in Figs. 1 and 2 of the main text, respectively.

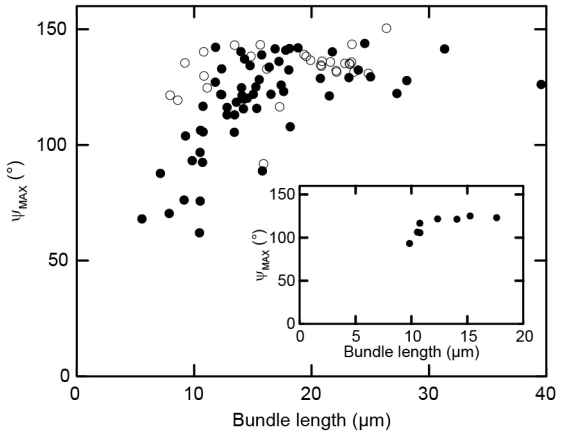

Extended Data Fig. 2 | Tangent-angle maximal amplitude as a function of bundle length. The beating bundles are driven by myosin II (black disks) or by myosin V (white disks). The inset shows the same relation for a single growing bundle driven by myosin II. In both cases, the maximal amplitude ψ_{MAX} of tangent-angle oscillation saturates beyond a bundle length of about 11 μm.

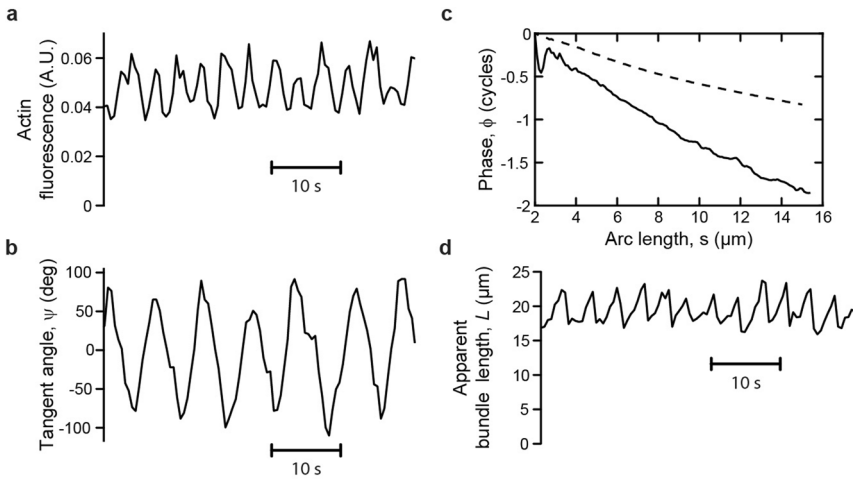

Extended Data Fig. 3 | Actin fluorescence blinking betrays out-of-the-plane beating. a, Oscillation of actin-fluorescence intensity (arbitrary units) as a function of time at the arc length s= 6 μm along the centre line of an actin-filament bundle. The period of oscillation is $T = 3.3$ s. **b**, Oscillation of the tangent angle ψ to the bundle's centre line as a function of time at the same arc length as in **a**. The period of oscillation is twice that of the fluorescence oscillation shown in **a**. **c**, Phase ϕ of the actin fluorescence oscillation (solid line) and of the tangent angle oscillation (dashed line) as a function of arc length s. The observed phase accumulation of fluorescence oscillation reveals propagation of a travelling wave with half the wavelength but with the same velocity, here 2.3 μm s^{-1}, as those of the corresponding actin-bending waves. **d**, Oscillation of the apparent bundle length L as a function of time, with the same period as that of fluorescence oscillations shown in **a**. The apparent bundle length is defined as the arc length of the bundle's tip that is detected in the actin-fluorescence image. This behaviour is interpreted as the consequence of a small out-of-the-plane component to the beat of the actin bundle, which modulates the measured intensity of actin fluorescence within the field depth of the spinning-disk microscope. The beating actin bundle was here driven by myosin II. See Supplementary Video 5 for an animated representation of the same data.

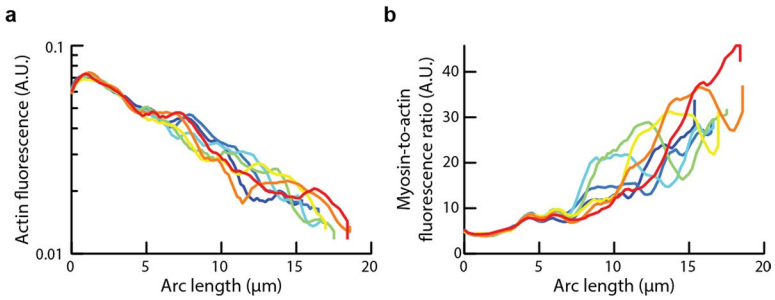

Extended Data Fig. 4 | Actin- and myosin-fluorescence profiles. a, Actin-fluorescence profiles along the centre line of a beating actin-filament bundle. **b**, Ratio of myosin-fluorescence and actin-fluorescence profiles. The order of the line colours, from dark blue to red, indicates time progression (time interval of 2 s); the profiles are plotted over one period of the myosin-density waves. Same beating actin bundle as in Figs. 2 and 4 in the main text.

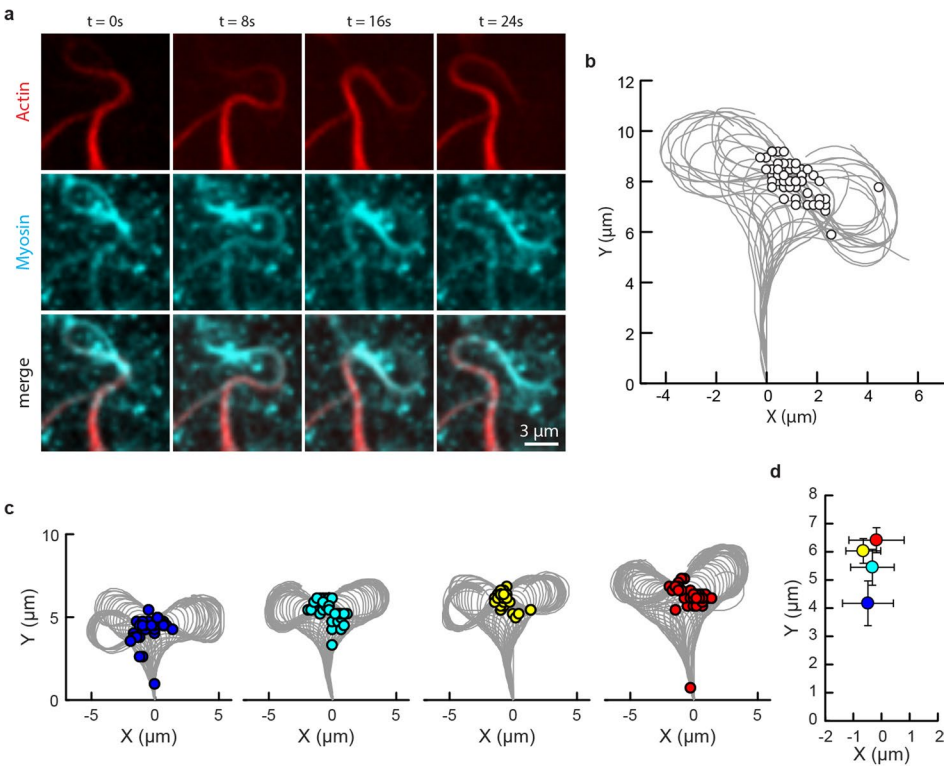

Extended Data Fig. 5 | Myosin localization within a beating actin bundle. a, Fluorescence images for actin (top row, in red) and myosin V (middle row, in cyan), as well as merged signals (bottom row), with an 8-s time interval over one period of the beat. **b**, Position of the myosin-density peak (disks) along the bundle's centreline (grey lines) as a function of time over 4.5 periods of the beat, with a sampling time of 2 s. Same bundle in **a**–**b** as in Figs. 2 and 4 in the main text. **c**, Same representation as in **b** for an actin-bundle that grows in time. The panels correspond to consecutive sections of a 137-s long recording, each lasting about 45 s. **d**, Mean position of the myosin-density peak for the data shown in each panel of **c**, with the corresponding colour code. Error bars are s.d. from the mean. The motors move vertically as the bundle grows, remaining near the centre of the figure-of-eight pattern of the actin beat. The data shown in **c**–**d** are associated with the Supplementary Video 9.

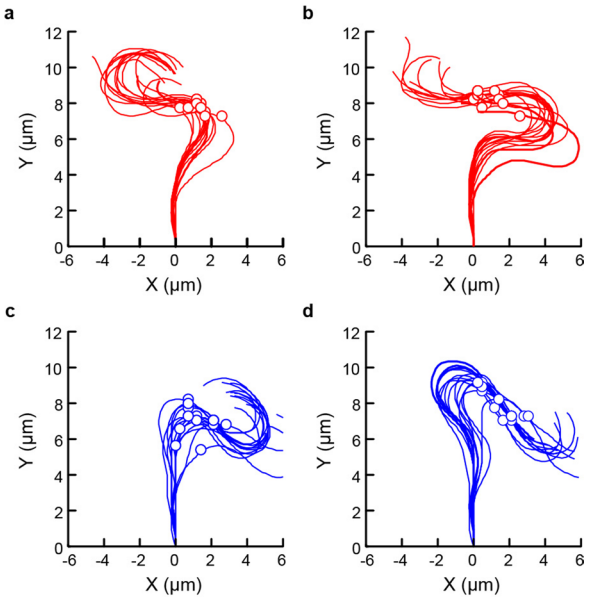

Extended Data Fig. 6 | Myosin peak position with respect to actin bundle curvature. a, At the initiation of a myosin-density wave, corresponding to the sudden appearance of a peak in the myosin-density profile along the bundle's centre line (Fig. 4a and d in the main text and Supplementary Video 7), the myosin-density peak (disks) is localized near an arc length of maximal positive curvature (Fig. 4e in the main text). **b**, A quarter period of tangent-angle oscillation later, here 8 s, the myosin-density peak is localized farther toward the bundle's tip, leaving the positively curved region of the actin-filament bundle behind. **c**, Half a period of tangent-angle oscillation after the initiation of the first myosin density wave, a second myosin-density wave is initiated at about the same arc length as in **a**, where curvature of the centre line is negative and near a local maximum of absolute value (see Fig. 4e in the main text). **d**, Eight seconds later, the myosin-density peak is localized farther toward the bundle's tip, leaving the negatively curved region behind. Same data as in Figs. 2 and 4 of the main text, for 14 successive periods of tangent-angle oscillations. Red (blue) lines correspond to the production of myosin-density waves associated with positive (negative) curvature of the actin-filament bundle.

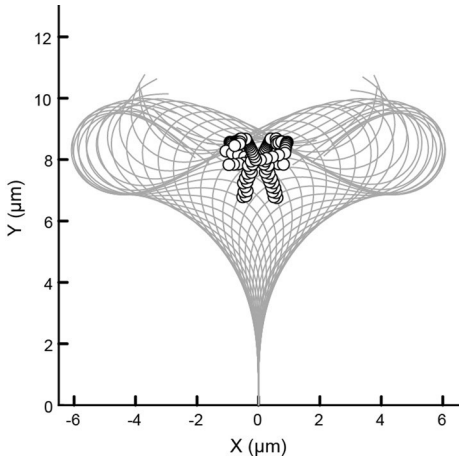

Extended Data Fig. 7 | Motor peak position (disks) on filament beating pattern (grey lines) in the model. Same data as in Fig. 5 of the Main Text and Supplementary Video 11; model parameter values in Supplementary Tables 1 and 2.

nature portfolio

Corresponding author(s): Pascal MARTIN

Last updated by author(s): Jun 13, 2022

Reporting Summary

Nature Portfolio wishes to improve the reproducibility of the work that we publish. This form provides structure for consistency and transparency in reporting. For further information on Nature Portfolio policies, see our Editorial Policies and the Editorial Policy Checklist.

Statistics

For all statistical analyses, confirm that the following items are present in the figure legend, table legend, main text, or Methods section.

n/a	Confirmed	
☐	☒	The exact sample size (*n*) for each experimental group/condition, given as a discrete number and unit of measurement
☐	☒	A statement on whether measurements were taken from distinct samples or whether the same sample was measured repeatedly
☐	☒	The statistical test(s) used AND whether they are one- or two-sided *Only common tests should be described solely by name; describe more complex techniques in the Methods section.*
☐	☒	A description of all covariates tested
☐	☒	A description of any assumptions or corrections, such as tests of normality and adjustment for multiple comparisons
☐	☒	A full description of the statistical parameters including central tendency (e.g. means) or other basic estimates (e.g. regression coefficient) AND variation (e.g. standard deviation) or associated estimates of uncertainty (e.g. confidence intervals)
☐	☒	For null hypothesis testing, the test statistic (e.g. *F*, *t*, *r*) with confidence intervals, effect sizes, degrees of freedom and *P* value noted *Give P values as exact values whenever suitable.*
☒	☐	For Bayesian analysis, information on the choice of priors and Markov chain Monte Carlo settings
☒	☐	For hierarchical and complex designs, identification of the appropriate level for tests and full reporting of outcomes
☐	☒	Estimates of effect sizes (e.g. Cohen's *d*, Pearson's *r*), indicating how they were calculated

Our web collection on statistics for biologists contains articles on many of the points above.

Software and code

Policy information about availability of computer code

Data collection	Time-lapse videos were aquired under the control of MetaMorph (version 7.8.13; Molecular Devices).
Data analysis	Data analysis was performed using the the ridge-detection plugin of the image-processing software ImageJ (as part of the package Fiji; NIH) and custom software written in Matlab (R2018a; the Mathworks). Numerical solutions to the model were obtained using custom software written in Python 3.

For manuscripts utilizing custom algorithms or software that are central to the research but not yet described in published literature, software must be made available to editors and reviewers. We strongly encourage code deposition in a community repository (e.g. GitHub). See the Nature Portfolio guidelines for submitting code & software for further information.

Data

Policy information about availability of data

All manuscripts must include a data availability statement. This statement should provide the following information, where applicable:

- Accession codes, unique identifiers, or web links for publicly available datasets
- A description of any restrictions on data availability
- For clinical datasets or third party data, please ensure that the statement adheres to our policy

The data that support the findings of this study are available from the corresponding author upon reasonable request.

Field-specific reporting

Please select the one below that is the best fit for your research. If you are not sure, read the appropriate sections before making your selection.

☒ Life sciences ☐ Behavioural & social sciences ☐ Ecological, evolutionary & environmental sciences

For a reference copy of the document with all sections, see nature.com/documents/nr-reporting-summary-flat.pdf

Life sciences study design

All studies must disclose on these points even when the disclosure is negative.

Sample size	We studied n=59 beating actin-filament bundles in m=13 experiments in the case with myosin-II motors and n=29 beating of actin-filament bundles in m=5 experiments with GFP-myosin-V motors. G-power analysis ensured that this sample size was sufficient to achieve a signal-to-noise ration of at least 0.65 with 80% power at a 5% significance level.
Data exclusions	Only actin-filament bundles that showed regular beating over at least 5 cycles and that could be tracked without interference with neighbors were included in the analysis.
Replication	Self-organized wave-like beating was observed in about 75% of our attemps, ensuring that the phenomenon is robust. Replication failed when passivation of the substrate was unsufficient.
Randomization	We considered two experimental groups, based on the molecular identity of the molecular motors driving the beating of actin-filament bundles, e.g. myosin-II vs myosin-V motors. Randomization is irrelevent to our in-vitro study.
Blinding	Blinding is irrelevant to our in-vitro study.

Reporting for specific materials, systems and methods

We require information from authors about some types of materials, experimental systems and methods used in many studies. Here, indicate whether each material, system or method listed is relevant to your study. If you are not sure if a list item applies to your research, read the appropriate section before selecting a response.

Materials & experimental systems

n/a	Involved in the study
☒	☐ Antibodies
☒	☐ Eukaryotic cell lines
☒	☐ Palaeontology and archaeology
☒	☐ Animals and other organisms
☒	☐ Human research participants
☒	☐ Clinical data
☒	☐ Dual use research of concern

Methods

n/a	Involved in the study
☒	☐ ChIP-seq
☒	☐ Flow cytometry
☒	☐ MRI-based neuroimaging